Targeting the potent Beclin 1–UVRAG coiled-coil interaction with designed peptides enhances autophagy and endolysosomal trafficking

Shuai Wu[a,b,1], Yunjiao He[a,c,d,1], Xianxiu Qiu[a,b,1], Wenchao Yang[a,b,e,2], Wenchao Liu[a,2], Xiaohua Li[a,b,3], Yan Li[f], Han-Ming Shen[g], Renxiao Wang[f], Zhenyu Yue[h], and Yanxiang Zhao[a,b,4]

[a]Department of Applied Biology and Chemical Technology, State Key Laboratory of Chirosciences, The Hong Kong Polytechnic University, Hung Hom, Kowloon, Hong Kong, People's Republic of China; [b]The Hong Kong Polytechnic University Shenzhen Research Institute, 518057 Shenzhen, People's Republic of China; [c]Department of Biology, Southern University of Science and Technology, 518055 Shenzhen, People's Republic of China; [d]Shenzhen Key Laboratory of Cell Microenvironment, Southern University of Science and Technology, 518055 Shenzhen, People's Republic of China; [e]Key Laboratory of Pesticide and Chemical Biology of the Ministry of Education, College of Chemistry, Central China Normal University, 430079 Wuhan, People's Republic of China; [f]State Key Laboratory of Bioorganic and Natural Products Chemistry, Shanghai Institute of Organic Chemistry, Chinese Academy of Sciences, 200032 Shanghai, People's Republic of China; [g]Department of Physiology, Yong Loo Lin School of Medicine, National University of Singapore, 117597 Singapore; and [h]Department of Neurology, The Friedman Brain Institute, Icahn School of Medicine at Mount Sinai, New York, NY 10027

Edited by Hao Wu, Department of Biological Chemistry and Molecular Pharmacology, Harvard Medical School, Boston, MA, and approved May 2, 2018 (received for review December 11, 2017)

The Beclin 1–Vps34 complex, known as "mammalian class III PI3K," plays essential roles in membrane-mediated transport processes including autophagy and endosomal trafficking. Beclin 1 acts as a scaffolding molecule for the complex and readily transits from its metastable homodimeric state to interact with key modulators such as Atg14L or UVRAG and form functionally distinct Atg14L/UVRAG-containing Beclin 1–Vps34 subcomplexes. The Beclin 1–Atg14L/UVRAG interaction relies critically on their coiled-coil domains, but the molecular mechanism remains poorly understood. We determined the crystal structure of Beclin 1–UVRAG coiled-coil complex and identified a strengthened interface with both hydrophobic pairings and electrostatically complementary interactions. This structure explains why the Beclin 1–UVRAG interaction is more potent than the metastable Beclin 1 homodimer. Potent Beclin 1–UVRAG interaction is functionally significant because it renders UVRAG more competitive than Atg14L in Beclin 1 binding and is critical for promoting endolysosomal trafficking. UVRAG coiled-coil mutants with weakened Beclin 1 binding do not outcompete Atg14L and fail to promote endolysosomal degradation of the EGF receptor (EGFR). We designed all-hydrocarbon stapled peptides that specifically targeted the C-terminal part of the Beclin 1 coiled-coil domain to interfere with its homodimerization. One such peptide reduced Beclin 1 self-association, promoted Beclin 1–Atg14L/UVRAG interaction, increased autophagic flux, and enhanced EGFR degradation. Our results demonstrate that the targeting Beclin 1 coiled-coil domain with designed peptides to induce the redistribution of Beclin 1 among its self-associated form or Atg14L/UVRAG-containing complexes enhances both autophagy and endolysosomal trafficking.

Beclin 1 | UVRAG | Atg14L | autophagy | endolysosomal trafficking

The mammalian class III PI3KC3 complex, also termed the "Beclin 1–Vps34 complex," is a dynamic multiprotein assembly that is indispensable in membrane-mediated intracellular transportation processes such as macroautophagy, endocytic trafficking, and phagocytosis (1). This complex contains four core members: catalytic lipid kinase Vps34 that serves as the major producer of phosphatidylinositol 3-phosphates (PI3Ps); serine/threonine kinase Vps15 that stably associates with Vps34; the scaffolding molecule Beclin 1; and Atg14L or UVRAG as mutually exclusive Beclin 1-binding partners (2, 3). The Atg14L-containing form is termed "complex I" (PI3KC3-C1) and is essential for early-stage autophagy induction because Atg14L is responsible for directing complex I to ER sites to promote autophagosome biogenesis (4–6). The UVRAG-containing form, on the other hand, is termed "complex II" (PI3KC3-C2) and plays critical roles in late-stage autophagosome maturation and degradative endolysosomal trafficking (7, 8). In addition to these core molecules, many regulators such as Ambra1, Bcl-2, NRBF2, and Rubicon can associate with the Atg14L- or UVRAG-containing Beclin 1–Vps34 complex in a dynamic and context-dependent manner to modulate the kinase activity of Vps34 (4, 5, 9–11). The molecular mechanism of such regulation, particularly how these molecules tune the activity of Vps34 through their interactions with members of the Beclin 1–Vps34 complex, is not well understood (1, 12).

Recent studies have provided extensive biochemical and structural information about the Beclin 1–Vps34 complexes. Negative-stain EM analysis of complex I at 28-Å resolution reveals a V-shaped

Significance

Beclin 1 is an essential autophagy protein. Through its coiled-coil domain, Beclin 1 recruits two modulators, Atg14L and UVRAG, to form Atg14L- or UVRAG-containing Beclin 1–Vps34 subcomplexes responsible for Vps34-dependent membrane trafficking processes including autophagy and endosomal trafficking. Our structural study of the Beclin 1–UVRAG coiled-coil complex reveals a strengthened interface to maintain potent Beclin 1–UVRAG interaction. This potency is essential for UVRAG to outcompete Atg14L and enhance Vps34-dependent endosomal trafficking. Our designed peptides can target the Beclin 1 coiled-coil domain, promote Atg14L– and UVRAG–Beclin 1 interaction, induce autophagy, and significantly enhance endolysosomal degradation of the EGF receptor. Our results testify to the feasibility of targeting Beclin 1 to regulate both autophagy and endosomal trafficking.

Author contributions: R.W., Z.Y., and Y.Z. designed research; S.W., Y.H., X.Q., W.Y., W.L., X.L., and Y.L. performed research; W.Y., H.-M.S., R.W., and Z.Y. contributed new reagents/analytic tools; S.W., Y.H., X.Q., W.Y., W.L., X.L., Y.L., R.W., Z.Y., and Y.Z. analyzed data; and S.W., X.Q., R.W., Z.Y., and Y.Z. wrote the paper.

Conflict of interest statement: The authors have filed patent applications in the United States and China based on this work.

This article is a PNAS Direct Submission.

Data deposition: The atomic coordinates and structure factors have been deposited in the Protein Data Bank, www.wwpdb.org (PDB ID code 5YR0).

[1]S.W., Y.H., and X.Q. contributed equally to this work.

[2]W.Y. and W.L. contributed equally to this work.

[3]Present address: Department of Research and Development, Shenzhen Benevop Biomedical Co., Ltd, 518110 Shenzhen, People's Republic of China.

[4]To whom correspondence should be addressed. Email: yanxiang.zhao@polyu.edu.hk.

This article contains supporting information online at www.pnas.org/lookup/suppl/doi:10.1073/pnas.1721173115/-/DCSupplemental.

Published online June 4, 2018.

architecture that is highly dynamic (13). In particular, the catalytic domain of Vps34 can become unhinged from the main body of the complex to adopt the catalytically active state (14). The crystal structure of the yeast homolog of complex II solved at 4.4-Å resolution shows a similar Y architecture, with Vps34 and Vps15 forming the catalytic arm and Atg30 and Atg38 (homologs of Beclin 1 and UVRAG) forming the regulatory arm (15). Although no side chains were modeled in the crystal structure due to limited resolution, hydrogen deuterium exchange analysis helped map certain regions of complex II that become more solvent exposed upon membrane binding (15). Furthermore, the negative-stained EM structure of mammalian NRBF2-containing complex I confirms that, as a positive regulator of Vps34, NRBF2 is located at the base of the V-shaped structure and can bridge two molecules of complex I via its C-terminal homodimeric coiled-coil domain (16). Interestingly, Atg38, the yeast homolog of mammalian NRBF2, binds to only a single molecule of complex I even though it forms a homodimer via its C-terminal coiled-coil domain as well (17). In summary, while the overall architecture and structural dynamics of Beclin 1–Vps34 complexes I and II have been investigated, the molecular mechanism by which modulating factors such as Atg14L, UVRAG, and NRBF2 bind to core members within the complex and exert their regulatory effect on Vps34 remains to be elucidated.

A notable and shared feature within the architecture of Beclin 1–Vps34 complex I and II is a parallel coiled-coil structure that runs through the regulatory arm comprising Beclin 1 and Atg14L or UVRAG. This structure corresponds to the key Beclin 1–Atg14 and –UVRAG interaction site at which Atg14L and UVRAG bind to Beclin 1 in mutually exclusive manner, targeting the same region within the coiled-coil domain. Cell biology and biochemical studies have shown that the coiled-coil domains of Beclin 1, Atg14L, and UVRAG are essential for maintaining their interaction because the deletion of any coiled-coil domain leads to loss of interaction as measured by immunoprecipitation (co-IP) experiments (4, 5, 13, 18).

Previously we determined the structure of the Beclin 1 coiled-coil domain and showed that it formed a metastable antiparallel coiled-coil assembly due to several charged or polar residues that destabilized an otherwise hydrophobic dimer interface (18, 19). Our biochemical data also reveal that Atg14L and UVRAG compete for the same binding site within the Beclin 1 coiled-coil domain and readily disrupt the Beclin 1 homodimer to form a heterodimeric Beclin 1–Atg14L or –UVRAG complex because they bind to Beclin 1 with higher affinity than Beclin 1's self-association (18, 19). We have proposed that a potent Beclin 1–Atg14L/UVRAG interaction may trigger the dynamic redistribution of Beclin 1 among its self-associated form or Atg14L/UVRAG-containing Beclin 1–Vps34 subcomplexes and serve as an important regulatory mechanism for Vps34-dependent processes, including autophagy and endolysosomal trafficking (18, 19). However, it is not known how the "imperfect" features of the Beclin 1 coiled-coil domain facilitate specific and potent interaction with Atg14L or UVRAG. Atomic details of these interactions cannot be extracted from the EM structure of complex I or from the crystal structure of yeast complex II due to limited resolution.

In this report, we present the crystal structure of the Beclin 1–UVRAG coiled-coil complex solved at 1.8-Å resolution and structure-based analysis to delineate the molecular determinants that underlie the formation of a stable Beclin 1–UVRAG complex. The functional significance of the potent Beclin 1–UVRAG interaction in mediating Vps34-dependent autophagy and endocytic trafficking is also investigated. Last, using the structures of the Beclin 1 coiled-coil domain and Beclin 1–UVRAG complex as guidance, we designed hydrocarbon-stapled peptides that could specifically bind to the Beclin 1 coiled-coil domain and enhance the Beclin 1–Atg14L and –UVRAG interactions to promote Vps34-dependent membrane trafficking processes including autophagy and endolysosomal degradation.

Results

The N-Terminal Region of the Beclin 1 Coiled-Coil Domain Is Most Important for Binding to Atg14L and UVRAG. Coiled-coil regions usually show a canonical sequence motif, a heptad repeat in the form of *abcdefg* with hydrophobic residues at positions *a* and *d*. Analysis of the heptad patterns in the putative coiled-coil regions of UVRAG and Atg14L residues reveals that they may contain two to three short coiled-coil fragments in contrast to the long and continuous stretch of coiled coil reported for Beclin 1 by our previous study (18). The crystal structure of yeast complex II also reveals that the long helix of Atg38 corresponding to its coiled-coil region contains a bend in the middle, effectively partitioning it into two shorter helices (15). It is not clear how the shorter coiled-coil segments found in Atg14L and UVRAG pair up with the long and continuous Beclin 1 coiled-coil domain to form a stable Beclin 1–Atg14L/UVRAG complex. It is possible that only certain regions within the Beclin 1 coiled-coil domain are of critical importance for interaction with Atg14L or UVRAG.

To map the exact Beclin 1 segment most important for interaction with Atg14L and UVRAG, we generated four Beclin 1 coiled-coil constructs (CC1–CC4), each seven heptad repeats long, to scan through the entire 13 heptad repeats of the Beclin 1 coiled-coil domain (Fig. 1*A*). The binding affinity of these constructs to the Atg14L and UVRAG coiled-coil regions was measured by an in vitro isothermal titration calorimetry (ITC) assay. ITC measurements reveal that CC1, i.e., the N-terminal half of the Beclin 1 coiled-coil domain (residues 178–227), binds to the UVRAG coiled-coil domain with a K_d of ∼7.6 μM, comparable to that for the entire Beclin 1 coiled-coil domain as reported in our previous study (Fig. 1*B*) (18). However, constructs CC2, CC3, and CC4 show no detectable interaction with UVRAG (Fig. 1*B*). A similar pattern of binding affinities is observed for the interaction with Atg14L: CC1 binds to Atg14L with an affinity (K_d of ∼29.3 μM) comparable to that of the full Beclin 1 coiled-coil domain reported in our previous study, but no interaction is observed for CC2, CC3, or CC4 (Fig. 1*C*). These studies confirm that the N-terminal part of the Beclin 1 coiled-coil domain as represented by

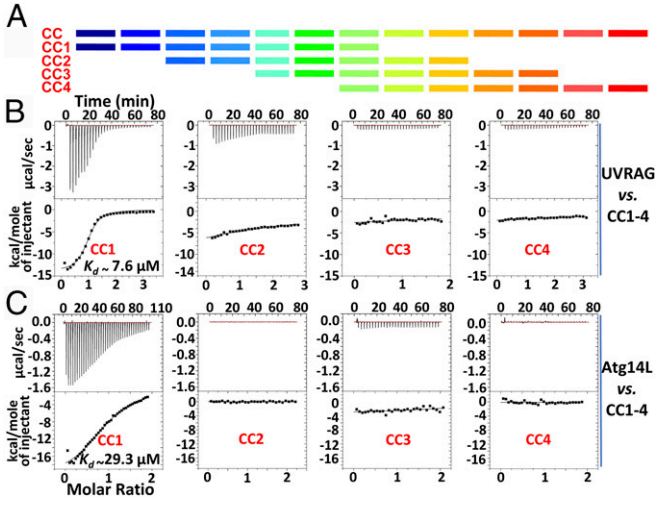

Fig. 1. The N-terminal region of the Beclin 1 coiled-coil domain is most critical for binding to UVRAG or Atg14L. (*A*) Design of constructs to map the region within the Beclin 1 coiled-coil domain most critical for binding to UVRAG or Atg14L. Four constructs, CC1–4, each consisting of seven heptad repeats, were designed to scan the entire Beclin 1 coiled-coil domain. Each heptad repeat is represented by a segment with a gradient color from the N terminus (dark blue) to the C terminus (dark red). (*B* and *C*) ITC profiles to measure the binding affinity of CC1–4 to the UVRAG (*B*) and Atg14L (*C*) coiled-coil regions. CC1 retains binding to UVRAG and Atg14L with a K_d comparable to that of the wild type.

the CC1 construct is the most critical region for interaction with Atg14L or UVRAG.

The Beclin 1–UVRAG Complex Structure Reveals a Coiled-Coil Interface Significantly Strengthened by Hydrophobic and Electrostatically Complementary Pairings. Our initial effort to crystallize the mixture of the Beclin 1 CC1 and the UVRAG coiled-coil fragment failed to produce any crystals. To circumvent this problem, we generated a series of "linked" constructs in which the Beclin 1 CC1 segment was tethered to the UVRAG coiled-coil fragment via a flexible $(GS)_5$ linker, and the length of the UVRAG fragment was varied to facilitate crystallization (*SI Appendix*, Fig. S1). These linked constructs were expected to form either an intra- or intermolecular Beclin 1–UVRAG coiled-coil complex to benefit crystallization. Indeed our ITC results confirmed that expectation, as no interaction was detected between the linked protein and either Beclin 1 or UVRAG, probably because the CC1 and UVRAG fragments within the linked protein were already engaged in forming the complex (*SI Appendix*, Fig. S2). One linked construct yielded crystals that diffracted to 1.8 Å at the synchrotron source, and the structure was determined by SIRAS (single isomorphous replacement with anomalous scattering) using Au as the heavy metal derivative (*SI Appendix*, Table S1).

The structure of the Beclin 1–UVRAG linked construct reveals a parallel heterodimeric coiled-coil assembly (Fig. 2*A*). Within the crystal lattice the Beclin 1–UVRAG complex was formed between two neighboring peptide chains with the Beclin 1 CC1 segment of one molecule matched up against the UVRAG coiled-coil region of a symmetry-related molecule nearby (*SI Appendix*, Fig. S3). No self-interactions for Beclin 1 CC1 or UVRAG were observed, and the flexible $(GS)_5$ linker was not visible. Close inspection of the structure yielded information on the molecular determinants that render the Beclin 1–UVRAG heterodimer more stable than the Beclin 1 homodimer. First, the Beclin 1–UVRAG complex contains a series of "perfect" *a*–*a*′ and *d*–*d*′ parings termed "leucine zippers" at the heterodimer interface to stabilize the parallel coiled-coil assembly (Fig. 2*B*). In fact, four such Beclin 1–UVRAG leucine zipper pairs, L178*d*–L232*d*′, L185*d*–L239*d*′, L192*d*–L246*d*′, and L196*a*–L250*a* (Beclin 1 residues are underlined), involve the same Beclin 1 residues that form similar hydrophobic *a*–*d*′ pairings in the Beclin 1 homodimer: L178*a*–L259*d*′, L185*a*–M252*d*′, L192*a*–L245*d*′, and L196*d*–L241*a*′ (Fig. 2*C*) (18).

Additionally, the Beclin 1–UVRAG complex contains several energetically favorable interacting pairs at its coiled-coil interface that replace the imperfect and destabilizing pairs seen in the Beclin 1 homodimer. There is one extra leucine zipper pair in the Beclin 1–UVRAG complex (L210*a*–L264*a*′) that replaces the corresponding imperfect pair (L210*a*–Y227*d*′) in the Beclin 1 coiled-coil homodimer (Fig. 2*D*). Furthermore, Beclin 1 residue R203 forms salt bridge interaction with UVRAG residue E260 at the heterodimer interface (Fig. 2*D*). This electrostatically complementary (R203*a*–E260*d*′) pairing effectively neutralizes the "destabilizing" effect exerted by the charged residues at the otherwise hydrophobic coiled-coil interface to facilitate stable association. By retaining all the perfect hydrophobic pairings and gaining additional stabilizing interactions, the Beclin 1–UVRAG complex is notably more stable than the Beclin 1 homodimer (Fig. 2*E*).

Furthermore, we tried to position our Beclin 1–UVRAG coiled-coil structure into that for the yeast complex II. Based on sequence alignment, the matching segment for Beclin 1 in yeast Atg30 (residues 215–280) covers approximately the N-terminal half of the Atg30 coiled-coil strand and ends right around the midpoint where the WD40 domain of Vps15 starts to impinge on the Atg30 coiled-coil region (*SI Appendix*, Fig. S4) (15). Interestingly, this midpoint region is also where the nearby coiled-coil strand of Atg38, i.e., the UVRAG homolog, bends slightly and breaks its α-helical structure (15). Thus, our Beclin 1–UVRAG structure likely represents the most essential and stable coiled-coil region within the Beclin 1–UVRAG regulatory arm of complex II. While Beclin 1, Atg14L, and UVRAG still adopt a helical structure beyond this region, they may not form a tightly packed coiled-coil assembly.

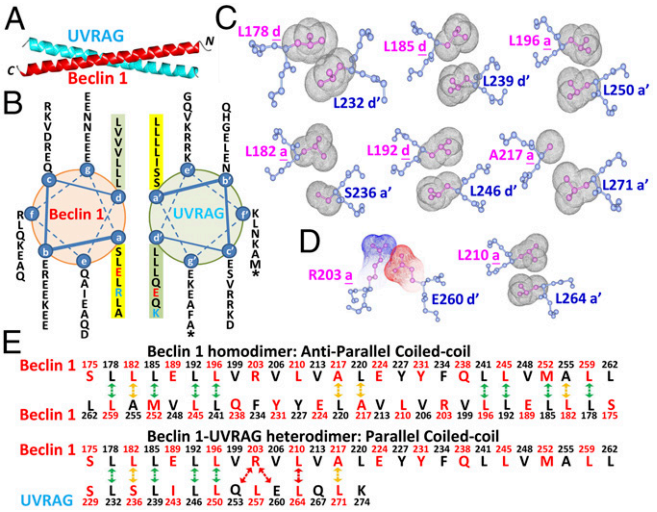

Fig. 2. The crystal structure of the Beclin 1–UVRAG coiled-coil complex reveals a significantly stabilized heterodimeric interface with both hydrophobic and electrostatically complementary pairings. (*A*) The parallel dimeric structure of the Beclin 1–UVRAG coiled-coil complex. N and C indicate the N- and C-terminal ends, respectively. (*B*) Helical wheel presentation of the Beclin 1–UVRAG coiled-coil dimer interface. (*C* and *D*) Close-up views of the hydrophobic and electrostatically complementary *a*–*a*′ and *d*–*d*′ pairings at the Beclin 1–UVRAG coiled-coil interface that are either similar to those found in the Beclin 1 homodimer (*C*) or are unique to the Beclin 1–UVRAG interface (*D*). (*E*) Comparison of the coiled-coil interfaces of the Beclin 1 homodimer and the Beclin 1–UVRAG heterodimer. The *a*–*d*′ pairings observed in the Beclin 1 homodimer and the *a*–*a*′/*d*–*d*′ pairings observed in the Beclin 1–UVRAG complex are aligned according to the Beclin 1 sequence. Green arrows mark the leucine zippers, orange arrows mark the moderately hydrophobic pairings, and red arrows mark the stabilizing pairings observed only in the Beclin 1–UVRAG complex.

The Potent Beclin 1–UVRAG Interaction Can Be Gradually Weakened by Mutations at Their Coiled-Coil Interface. As our structure reveals a significantly stabilized coiled-coil interface for the Beclin 1–UVRAG interaction, we set out to test whether this potent interaction can be gradually weakened if key hydrophobic or electrostatically complementary pairings at the interface are mutated. This would also serve to validate our structure obtained using Beclin 1 and UVRAG fragments instead of the full-length proteins.

We first generated a series of Beclin 1 mutants and measured their binding affinity to the UVRAG coiled-coil region in vitro (Fig. 3*A* and *SI Appendix*, Table S2). Mutations involving residues R203 and L210 perturb the additional pairings unique to the Beclin 1–UVRAG complex, while mutations involving L178, L185, L192, and L196 perturb the canonical leucine zipper pairs common between the Beclin 1–UVRAG heterodimer and the Beclin 1 homodimer. We also generated quintuple mutations (5L5A and 5L5E) that mutate all leucine residues at the Beclin 1–UVRAG interface. Our in vitro ITC binding results show that single mutations such as R203E and L210E reduce the binding affinity of the Beclin 1–UVRAG interaction modestly, by approximately three- to fivefold (K_d ~10 μM vs. ~3 μM for the wild type) (*SI Appendix*, Table S2). Double mutations such as R203E_L210E and L192A_L196A further weaken the Beclin 1–UVRAG interaction, with the K_d decreasing to 15–30 μM. Only the quintuple mutations 5L5A and 5L5E completely abolished the Beclin 1 and UVRAG coiled-coil regions.

We also did similar characterization of UVRAG by mutating one, two, five, or all six of the leucine residues that are involved in forming leucine zipper pairings at the Beclin 1–UVRAG coiled-coil interface to glutamate (Fig. 3*B* and *SI Appendix*, Table S3). The single Leu-to-Glu mutation L246E (hereafter, "1E") weakened the Beclin 1–UVRAG interaction significantly with a K_d of ~139 μM vs. ~0.3 μM for the wild type. Mutating

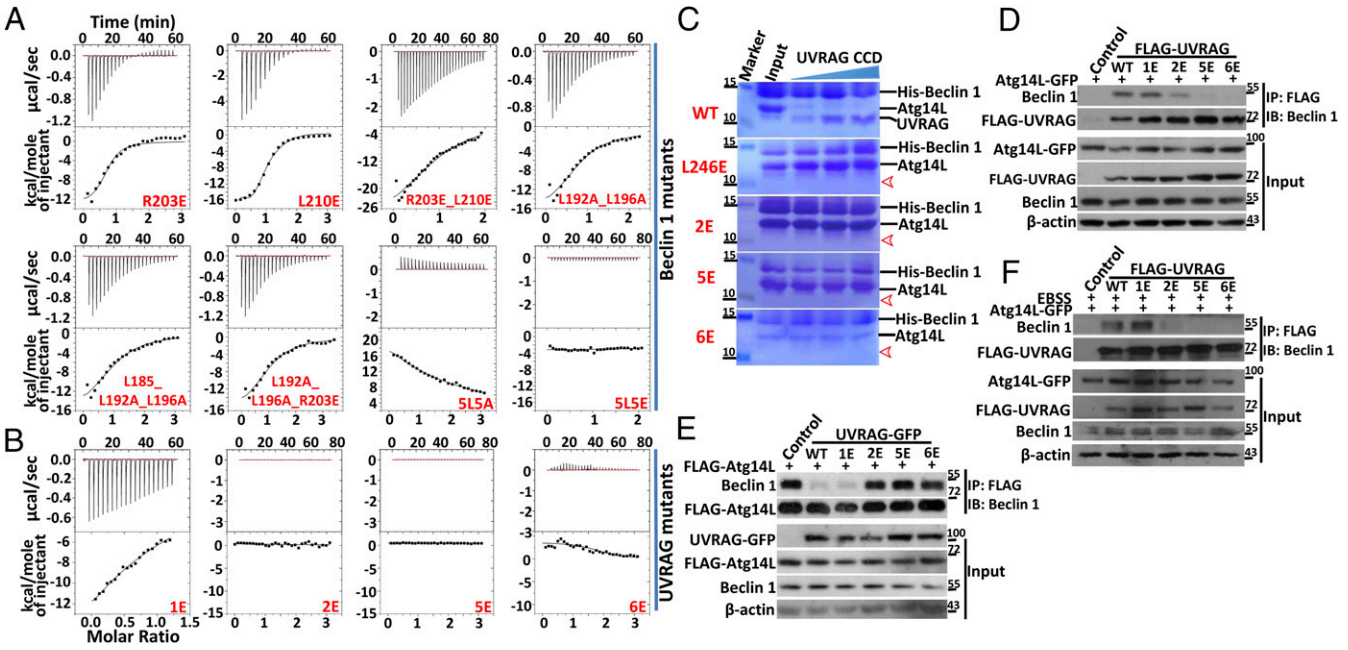

Fig. 3. The potent Beclin 1–UVRAG interaction can be gradually weakened by mutations at its coiled-coil interface, leading to the loss of a competitive advantage over the Beclin 1–Atg14L interaction. (*A* and *B*) ITC profiles measuring the binding affinity of Beclin 1 mutants to UVRAG (*A*) and of UVRAG mutants to Beclin 1 (*B*). (*C*) In vitro pull-down assay when UVRAG constructs were titrated to the preformed Beclin 1–Atg14L coiled-coil complex. The arrowheads indicate the expected position of the eluted UVRAG construct. (*D*) Co-IP experiments to assess the impact of UVRAG mutations on its competitive advantage against Atg14L in binding to Beclin 1 in vivo. The FLAG-UVRAG constructs and GFP-Atg14L were cotransfected into HEK293T cells. The interaction between FLAG-UVRAG mutants and endogenous Beclin 1 in the presence of overexpressed Atg14L-GFP as competitor was probed using anti–FLAG-M2 magnetic beads for immunoprecipitation (IP), followed by immunoblotting (IB) using anti-Beclin 1 antibody. (*E*) Competitive co-IP experiments similar to those in *D*. The tags for UVRAG mutants and Atg14L were swapped. (*F*) Repetition of the competitive co-IP experiment in *D* under amino acid/serum starvation conditions for 2 h [Earle's Balanced Salt Solution (EBSS+)].

two, five, or all six leucine residues to glutamate (2E, 5E, and 6E, respectively) completely abolishes its binding to Beclin 1.

Overall, our mutational studies confirm that the hydrophobic and electrostatically complementary pairings identified from our crystal structure are indeed critical for the Beclin 1–UVRAG interaction. Collaboratively they render the Beclin 1–UVRAG coiled-coil interaction highly potent, as multiple mutations are required to significantly weaken or completely abolish this interaction.

UVRAG Coiled-Coil Mutations Compromise Its Competitive Advantage over Atg14L in Recruiting Endogenous Beclin 1. Our previous study has shown that UVRAG is a stronger binding partner for Beclin 1 than Atg14L in vitro and outcompetes Atg14L in recruiting endogenous Beclin 1 to the UVRAG-containing complex when overexpressed in vivo (18). Furthermore, studies by Liang et al. (8) have shown that overexpression of UVRAG leads to enhanced endolysosomal trafficking as confirmed by assays that measure EGF-stimulated endocytic transport and lysosomal degradation of the EGF receptor (EGFR). With our structure-based UVRAG coiled-coil mutants that show weakened or abolished binding to Beclin 1 in vitro, we set out to test whether the potency of the Beclin 1–UVRAG coiled-coil interaction would be critical for its competitive advantage over Atg14L and for its function in promoting endolysosomal trafficking.

We first conducted in vitro pull-down experiments in which increasing amounts of UVRAG coiled-coil constructs were titrated to the preformed Beclin 1–Atg14L coiled-coil complex. As shown in Fig. 3*C*, the wild-type UVRAG coiled-coil construct readily outcompeted Atg14L and could be pulled down by the His-tagged Beclin 1 coiled-coil domain. However, UVRAG mutants such as 1E, 2E, 5E, and 6E all failed to do so. This result confirms that the competitive advantage of UVRAG over Atg14L in binding Beclin 1 relies critically on the hydrophobic residues within its coiled-coil domain.

We also performed co-IP experiments to assess the interaction between overexpressed UVRAG mutants and endogenous Beclin 1. FLAG-tagged UVRAG (FLAG-UVRAG) 1E, 2E, 5E, and 6E constructs were transfected into HEK293T cells. Co-IP was carried out using magnetic beads conjugated with anti-FLAG antibody, and the amount of endogenous Beclin 1 pulled down by FLAG-UVRAG was assessed by Western blot. Our data show that the 1E, 2E, 5E, and 6E constructs pull down approximately equal amounts of endogenous Beclin 1 regardless of the number of Leu-to-Glu mutations (*SI Appendix*, Fig. S5). This result suggests that Leu-to-Glu mutations that weaken or disrupt the Beclin 1–UVRAG coiled-coil interaction in vitro are not sufficient to abolish their association in vivo, probably because of the presence of other binding partners such as Vps34 and Vps15. In fact, the crystal structure of yeast complex II shows that the N-terminal C2 domain of Atg38 interacts with Vps15 at the base of the Y-shaped architecture (15). Additionally, the C-terminal BARA domain of Atg30 packs closely against the C-terminal BARA-like domain of Atg38 (15). Similar interactions can also be inferred in the negative-stained EM structures of mammalian complex I and II (13). Thus, the UVRAG-containing Beclin 1–Vps34 complex can still be assembled in vivo even though the Beclin 1–UVRAG coiled-coil interaction is weakened or abolished.

To assess the functional significance of the potent Beclin 1–UVRAG coiled-coil interaction, we then used competitive co-IP experiments to evaluate the impact of the Leu-to-Glu mutations 1E, 2E, 5E, and 6E on UVRAG's competitive advantage over Atg14L in recruiting endogenous Beclin 1. FLAG-UVRAG mutants and GFP-tagged wild-type Atg14L (Atg14L-GFP) were cotransfected into HEK293T cells under normal conditions. Co-IP was then conducted using magnetic beads conjugated with anti-FLAG antibody, and the amount of endogenous Beclin 1 pulled down by FLAG-UVRAG was assessed by Western blot. Our results show that in the presence of overexpressed Atg14L, the 1E

and 2E UVRAG constructs pulled down amounts of endogenous Beclin 1 similar to that pulled down by wild-type UVRAG, suggesting that they bind to Beclin 1 with stronger affinity and can outcompete Atg14L (Fig. 3*D*). In contrast, the amount pulled down by the 5E mutation was significantly reduced, and the 6E mutation barely pulled down any detectable amount (Fig. 3*D*).

To confirm this result, we conducted reverse competitive co-IP by swapping the tags on Atg14L and UVRAG and cotransfecting FLAG-Atg14L and UVRAG-GFP mutants into HEK293T cells under normal conditions. Similarly, Atg14L could not pull down Beclin 1 in the presence of overexpressed wild-type UVRAG and the 1E construct (Fig. 3*E*). However, Atg14L did outcompete the 2E, 5E, and 6E constructs and pulled down a significant amount of endogenous Beclin 1 (Fig. 3*E*). Interestingly, the 2E construct appeared to bind to Beclin 1 with affinity comparable to that of Atg14L because both Atg14L- and UVRAG(2E)-containing Beclin 1 complexes could be detected in the two rounds of competitive co-IP experiments (Fig. 3 *D* and *E*).

We further repeated the competitive co-IP experiment under autophagy-inducing conditions by subjecting the cotransfected HEK293T cells to 2 h of amino acid/serum starvation before lysing them for co-IP. A similar immunoprecipitation pattern was observed. In the presence of overexpressed Atg14L-GFP, the wild-type FLAG-UVRAG and the 1E mutant pulled down significant amounts of endogenous Beclin 1, while the 5E and 6E mutants failed to do so (Fig. 3*F*). Notably, the 2E construct did not pull down any detectable amount of Beclin 1 under starvation conditions, although it could do so under normal conditions (Fig. 3*F*). Previous studies have shown that starvation promotes the formation of the Atg14L-containing Beclin 1–Vps34 complex through AMPK-mediated phosphorylation of Beclin 1 (20). Given that Atg14L and UVRAG(2E) bind to Beclin 1 with comparable affinity under normal conditions, our data imply that starvation treatment may effectively partition more endogenous Beclin 1 into the Atg14L-containing complex at the expense of UVRAG(2E).

These in vitro and in vivo competitive-binding results confirm that the potency of the Beclin 1–UVRAG coiled-coil interaction is critical for UVRAG to outcompete Atg14L in recruiting endogenous Beclin 1. Leu-to-Glu mutations in the UVRAG coiled-coil domain that weaken the potent Beclin 1–UVRAG interaction render UVRAG less or noncompetitive against Atg14L.

The Potent Beclin 1–UVRAG Interaction Is Not Critical for Autophagy but Is Essential for Endolysosomal Trafficking. As our structural and biochemical data confirm that the potent Beclin 1–UVRAG coiled-coil interaction ensures the competitive advantage of UVRAG over Atg14L in recruiting endogenous Beclin 1, we set out to understand whether this competitiveness would affect Vps34-dependent membrane-trafficking processes, including autophagy and endolysosomal trafficking.

We transfected wild-type UVRAG and the 1E–6E mutants into HeLa cells and assessed their impact on autophagic activity by Western blots of LC3, the autophagy marker that converts from the nonlipidated form LC3-I to become the autophagosome-associated lipidated form LC3-II. Overexpression of UVRAG caused little change in the level of LC3-II, regardless of the presence or absence of the lysosomal inhibitor chloroquine (CQ) (Fig. 4*A*). Similar results were observed in HEK293T cells, where overexpression of wild-type UVRAG and the multiple Leu-to-Glu mutants did not change the total amount of LC3-II in either the

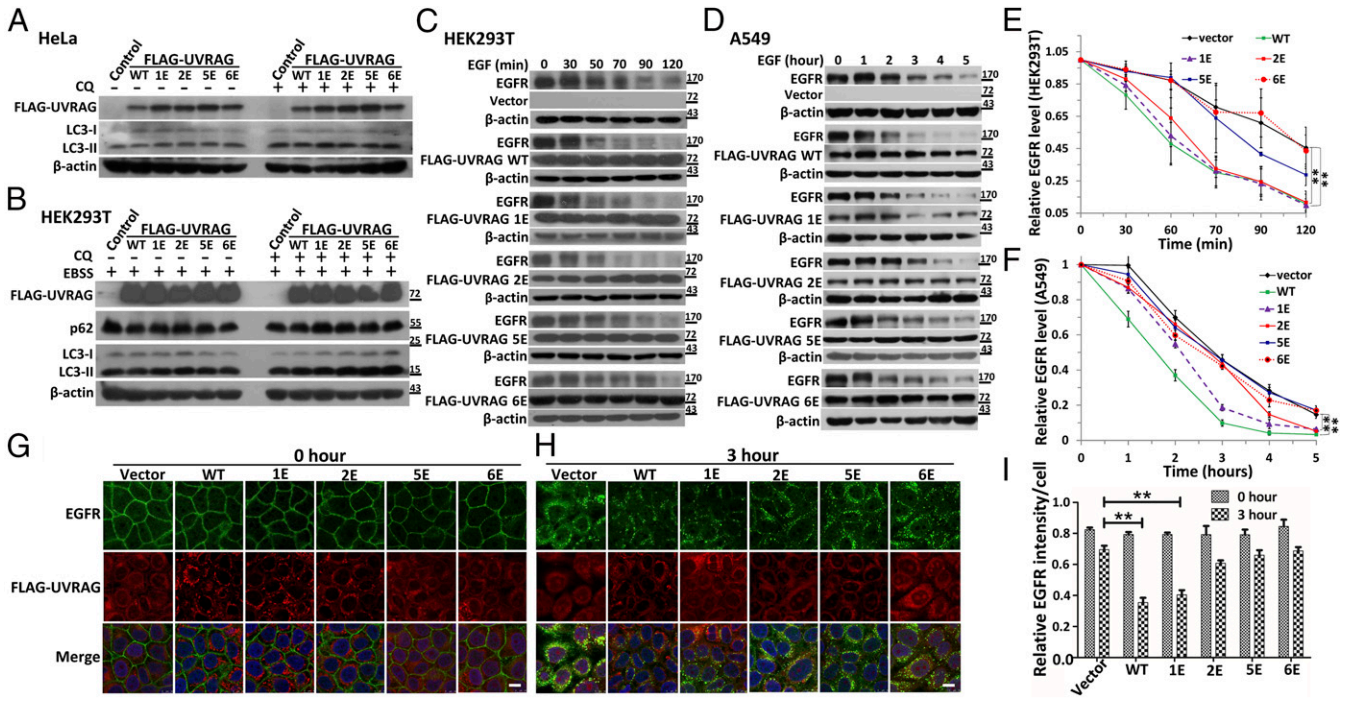

Fig. 4. The potent Beclin 1–UVRAG interaction is of limited benefit for autophagy but is essential for endolysosomal trafficking. (*A*) Western blots of the autophagy marker LC3 in HeLa cells transfected with FLAG-UVRAG wild-type (WT) or mutant constructs (1E, 2E, 5E, and 6E) for 48 h without (–) or with (+) CQ (25 μM) treatment for 3 h. (*B*) Repetition of experiments in *A* using HEK293T cells under amino acid/serum starvation for 2 h [Earle's Balanced Salt Solution (EBSS+)]. (*C* and *D*) The impact of UVRAG Leu-to-Glu mutations on the EGFR degradation profile in HEK293T (*C*) and A549 (*D*) cells. After transfection with UVRAG constructs, HEK293T and A549 cells were serum-starved overnight and treated with 200 ng/mL EGF. The EGFR level in the cell lysate was analyzed by Western blot at specific time points. (*E* and *F*) Time-dependent plots to quantify the EGFR degradation profile in HEK293T cells (*E*) and A549 cells (*F*). Data are from three separate experiments in each cell type. The level of EGFR was first normalized to the β-actin level at different time points and was further normalized to time 0, when ligand EGF was added. Values represent the mean ± SEM of three independent experiments; *P, 0.05, **P, 0.01; t test. (*G* and *H*) Immunofluorescence imaging of EGFR in A549 cells before (0 h) (*G*) and after (3 h) (*H*) EGF treatment. After same transfection and EGF treatment as in *C* and *D*, cells were blocked and incubated with anti-EGFR and anti-FLAG primary antibodies, respectively, followed by incubation with anti-rabbit and anti-mouse Alexa Fluor secondary antibodies. (Scale bar: 10 μm.) (*I*) EGFR fluorescence intensity per cell was analyzed and quantified by ImageJ (NIH). Bars represent the mean ± SEM of three independent experiments; *P, 0.05, **P, 0.01; t test.

presence or absence of CQ (Fig. 4*B*). We also assessed the expression level of p62, the receptor and substrate for selective autophagy. Overexpression of different UVRAG constructs did not change the amount of p62, either (Fig. 4*B*). These results suggest that neither wild-type UVRAG nor the mutants with weakened or abolished Beclin 1–UVRAG coiled-coil interaction exert any dominant effect on the autophagy process. This finding is in agreement with a previous study in which the positive effect of UVRAG overexpression in promoting autophagy in human HCT116 colon cancer cells was prominent only under stable transfection conditions (7). Notably, because of a truncation mutation, HCT116 cells have a significantly lower level of endogenous UVRAG than HEK293T or HeLa cells that express normal amounts of endogenous UVRAG (7).

Besides its role in the autophagy process, UVRAG also has been shown to be important for endocytic trafficking and delivery to lysosomes, either through the UVRAG-containing Beclin 1–Vps34 complex or through its interaction with the class C Vps complex (3, 8). However, it is not clear whether UVRAG's role in endocytic trafficking requires a potent Beclin 1–UVRAG interaction. To address this question, we monitored the process of EGF-stimulated endocytic transport and lysosomal degradation of EGFR in HEK293T cells after transient overexpression of wild-type UVRAG and the Leu-to-Glu mutants. As our data show, overexpression of wild-type UVRAG and the 1E and 2E constructs led to significantly enhanced EGFR degradation, with only ∼65% EGFR remaining at 60 min post EGF stimulation and ∼10% detected by 120 min. This is in contrast to more than 85% remaining at 60 min and ∼45% remaining at 120 min under vector-expressing conditions (Fig. 4 *C* and *E*). The overexpression of 5E showed little impact on EGFR degradation for the first 60 min but did enhance this process noticeably at 90 and 120 min (Fig. 4 *C* and *E*). In contrast, 6E caused no change, as its EGFR degradation profile was largely identical to that of the vector-expressing condition (Fig. 4 *C* and *E*).

We also conducted similar experiments using the A549 non-small cell lung cancer (NSCLC) cell line that overexpresses EGFR and is sensitive to tyrosine kinase inhibitors (TKIs) such as gefitinib. The rate of EGFR degradation in these cells is significantly prolonged compared with that in HEK293T cells (half-life ∼3 h vs. ∼1 h), probably to sustain excessive proliferation (Fig. 4 *D* and *F*). Nonetheless, the overexpression of wild-type UVRAG in A549 cells significantly enhanced the degradation profile of EGFR, with only ∼40% and ∼5% remaining after 3 and 5 h, respectively. In contrast, under the vector-expressing condition, ∼70% of EGFR was detected after 3 h, and ∼20% was detected after 5 h (Fig. 4 *D* and *F*). The 1E construct showed an enhancement effect, too, although it was weaker than that of wild-type UVRAG (∼50% and ∼5% after 3 and 5 h, respectively) (Fig. 4 *D* and *F*). The other Leu-to-Glu constructs, including 2E, 5E, and 6E, produced little enhancing effect, as their EGFR degradation rate was largely identical to the degradation rate under the vector-expressing condition (Fig. 4 *D* and *F*).

To further characterize the impact of UVRAG on EGFR endocytic trafficking and lysosomal degradation, we conducted immunofluorescence imaging of endogenous EGFR in A549 cells upon transfection of different UVRAG constructs. Our data show that before EGF treatment, endogenous EGFR is located almost exclusively on the well-defined thin layer of the plasma membrane, regardless of the UVRAG construct transfected (Fig. 4*G*). However, for all constructs, at 3 h after EGF treatment nearly all endogenous EGFR became internalized, puncta-like structures appeared in the cytosol, and the sharp boundary of the plasma membrane outlined by EGFR largely disappeared (Fig. 4*H*). There are clear differences in EGFR degradation for the different UVRAG constructs. The overexpression of UVRAG constructs with strong binding to Belin 1, i.e., the wild type and the 1E mutant, led to the most significant loss of endogenous EGFR (from ∼0.8 to ∼0.4 in terms of relative intensity per cell) (Fig. 4 *H* and *I*). In contrast, overexpression of UVRAG mutants that have weakened binding to Beclin 1, such as 2E, 5E, and 6E, caused significantly less EGFR degradation (from ∼0.8 to ∼0.6–0.7), similar to that for empty vector (Fig. 4 *H* and *I*).

In summary, our data show that overexpression of wild-type UVRAG and Leu-to-Glu mutants has little effect on the autophagy process in cell lines that have normal autophagic activity. Such overexpression does enhance endolysosomal trafficking but requires potent Beclin 1–UVRAG interaction because only wild-type UVRAG and the Leu-to-Glu mutants 1E and 2E lead to noticeably faster EGFR degradation, while the 5E and 6E mutants cannot induce any beneficial effect.

Structure-Based Design of Stapled Peptides That Reduce Beclin 1 Self-Association and Enhance Beclin 1–Atg14L/UVRAG Interaction. Our structural findings so far demonstrate that the potent Beclin 1–UVRAG coiled-coil interaction relies on a heterodimeric interface that is significantly more stable than the imperfect and metastable Beclin 1 coiled-coil homodimer. Our cell-based assays also show that the potency of the Beclin 1–UVRAG coiled-coil interaction is critical for promoting Vps34-dependent endocytic trafficking and lysosomal degradation of EGFR. We were motivated to design small-molecule compounds that could target the Beclin 1 coiled-coil domain and enhance the Beclin 1–UVRAG interaction in vivo. Such molecules, if successful, can serve not only as effective investigative tools to delineate the functional role of Beclin 1–Atg14L and Beclin 1–UVRAG interactions but also as lead compounds to augment autophagy and other Vps34-depepdent processes.

To enhance the Beclin 1–UVRAG interaction in vivo, we reasoned that a practical approach would be to reduce Beclin 1 self-association so that more endogenous Beclin 1 could be recruited by Atg14L or UVRAG to form Atg14/UVRAG-containing Beclin 1–Vps34 complexes. Following this design principle, we decided to use an 11-residue segment corresponding to residues 191–205 within the Beclin 1 coiled-coil domain as the template for our designed compounds (Fig. 5*A*). This template is expected to associate with the C-terminal end of the Beclin 1 coiled-coil domain, i.e., residues 231–245 according to our Beclin 1 coiled-coil homodimer structure, so that it could disrupt Beclin 1 self-association. However, it is not expected to compete with UVRAG for Beclin 1 interaction because its target site on Beclin 1 does not overlap with the target site for UVRAG. Furthermore, this template is also not expected to outcompete the full Beclin 1 coiled-coil domain in binding to UVRAG.

Our Beclin 1-derived template segment is expected to adopt an α-helical structure to bind to the Beclin 1 coiled-coil domain. However, its short length of 11 residues may not favor such secondary structure due to thermodynamics. Indeed our initial trials using unmodified peptides failed to detect any binding to Beclin 1. To solve this problem, we decided to modify the template by adding hydrocarbon stapling to reinforce the α-helical structure. This method has been shown to be an effective approach to design peptide mimetics that form short α-helices to modulate protein–protein interactions (21, 22). Besides, hydrocarbon stapling has been found to enhance the cell permeability of the peptide mimetics as well (23).

With the target-binding site of residues 231–245 defined, we proceeded to the design of a small library of stapled peptides. The model of the first stapled peptide (SP1) was built by simply taking the α-helical segment that interacts with the target region within the Beclin 1 homodimer structure, i.e., the segment covering residues 191–205, as the prototype. A hydrocarbon staple of 11-carbon length was introduced in silico to connect residues 197 and 204 via (i, $i + 7$) linkage that spanned two helical turns. With both residues located on the outer side of the helix and not involved in the coiled-coil interface, the formed staple was expected only to help stabilize the α-helical structure but not to interfere with Beclin 1 binding. The structural model of the SP1–Beclin 1 interaction was generated by superposing SP1 onto the Beclin 1 coiled-coil homodimer structure (Fig. 5*B*). Computational optimization to enhance the binding affinity of SP1 was carried out. A library of stapled peptides (SP2–SP12) was generated in which residues deemed critical for target-site binding were unchanged

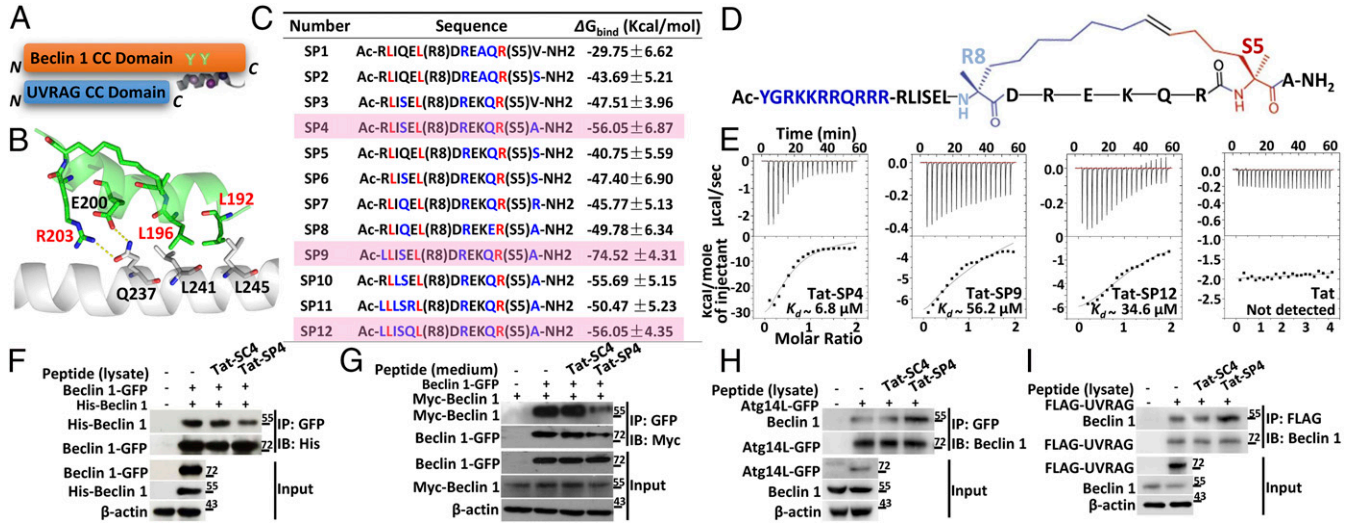

Fig. 5. Structure-based rational design of stapled peptides to target the Beclin 1 coiled-coil domain and promote Beclin 1–UVRAG interaction (*A*) The design principle of Beclin 1-specific α-helical stapled peptides. The peptide is shown as a short ribbon that binds to the C-terminal half of the Beclin 1 coiled-coil domain. The spheres represent the hydrocarbon staples that stabilize the α-helical structure. (*B*) Model of the designed stapled peptide SP1 binding to the C-terminal region of the Beclin 1 coiled-coil domain. Dashed lines mark the hydrogen bonds. Residues are numbered according to the Beclin 1 sequence. (*C*) A list of computationally designed stapled peptides. Modified residues are colored blue; residues colored red or black remain unchanged. R8 and S5 represent two residues that were chemically modified to form the hydrocarbon linkage. Three highlighted candidates, SP4, SP9, and SP12 show significantly improved theoretical interaction energy compared with SP1. (*D*) Sequence and chemical structure of Tat-SP4. The Tat signal peptide (colored in blue) is added to facilitate cell penetration. (*E*) ITC profile to measure the interaction between Beclin 1 and designed peptides. (*F*) Tat-SP4 reduces Beclin 1 self-association in vivo. GFP- and His-tagged Beclin 1 were cotransfected into HEK293T cells, and their self-association was probed by co-IP. Tat-SC4 and Tat-SP4 were added to the cell lysate at a 20-μM concentration before the immunoprecipitation procedure. Tat-SC4 is a control peptide with a scrambled Tat-SP4 sequence and without the hydrocarbon staple. (*G*) Repeat of the co-IP experiment in *F* but with Tat-SC4 and Tat-SP4 added to the cell culture medium at 20 μM 6 h posttransfection. (*H* and *I*) Tat-SP4 promotes the Beclin 1–Atg14L/UVRAG interaction in vivo. GFP-Atg14L (*H*) and FLAG-UVRAG (*I*) were transfected into HEK293T cells, and their interaction with endogenous Beclin 1 was probed by co-IP. Tat-SC4 and Tat-SP4 were added to the cell lysate at a 20-μM concentration before the immunoprecipitation procedure.

while other amino acid residues were computationally mutated (Fig. 5*C*). The binding modes of these stapled peptides to the Beclin 1 molecule were characterized by molecular dynamics simulations, and their binding energies were computed using the force field-based molecular mechanics generalized born surface area (MM-GB/SA) method. Certain sequence changes, such as replacing Gln194 with Ser and Val205 with Ala in SP4, SP9, and SP12, led to significantly improved binding energy (Fig. 5*C*).

For optimized SP4, SP9, and SP12, we decide to synthesize two modified versions (*SI Appendix*, Table S4). First, to enhance solubility and improve cell penetration, we decided to add the Tat sequence of YGRKKRRQRRR at the N terminus to synthesize Tat-SP4, Tat-SP9, and Tat-SP12. Second, for imaging studies we chose to add a Rhodamine B label at the N terminus to produce Rho-SP4, Rho-SP9, and Rho-SP12. Synthesis of these peptides (Fig. 5*D*) was carried out by a commercial vendor following the method pioneered by Kim et al. (24). The purified products were confirmed by mass spectroscopy and HPLC with good solubility (*SI Appendix*, Fig. S6). The ITC profile showed a direct interaction between Tat-SP4 and the Beclin 1 coiled-coil domain with a K_d of ∼6.8 μM, suggesting that this molecule can bind to the Beclin 1 coiled-coil domain effectively (Fig. 5*E*). Tat-SP9 and Tat-SP12 also interact with the Beclin 1 coiled-coil domain, although with lower binding affinities of ∼56.2 μM and ∼34.6 μM, respectively (Fig. 5*E*). The Tat peptide alone does not bind to Beclin 1, confirming that our design strategy of adding it to the stapled peptides does not interfere with Beclin 1 interaction (Fig. 5*E*).

We then conducted co-IP experiments to probe whether these designed peptides can disrupt Beclin 1 self-association and promote the Beclin 1–Atg14L/UVRAG interaction in vivo. Tat-SP4 was used for this study because it showed the strongest binding affinity to Beclin 1 in vitro. GFP- and His-tagged Beclin 1 was cotransfected into HEK293T cells, and 20 μM Tat-SP4 was added to the cell medium 6 h posttransfection or to the cell lysate after lysis. The self-association between GFP- and His-tagged Beclin 1 was then probed by co-IP. Our data show that, when added to the cell lysate, Tat-SP4 moderately reduced the amount of His-Beclin 1 pulled down by GFP-Beclin 1, suggesting that Beclin 1 self-association was reduced (Fig. 5*F*). The reduction of Beclin 1 self-association was more prominent when Tat-SP4 was added directly to the cell medium (Fig. 5*G*). This is likely due to a dosage effect, because more Tat-SP4 was used to maintain the same 20-μM concentration in 10 mL of cell medium than in 200 μL of cell lysate. In contrast, no such reduction was observed when cells were treated with Tat-SC4, a control peptide with an N-terminal Tat fragment and a scrambled SP4 sequence, at same concentration. The impact of Tat-SP4 on the Beclin 1–Atg14L/UVRAG interaction was assessed by co-IP experiments as well. Atg14L-GFP was transfected into HEK293T cells, and its interaction with endogenous Beclin 1 was probed by co-IP after Tat-SC4 or Tat-SP4 was added to cell lysate. Our data show that Tat-SP4 significantly enhanced the amount of endogenous Beclin 1 pulled down by Atg14L-GFP, but no such enhancement was observed for Tat-SC4 (Fig. 5*H*). A similar effect was observed for the Beclin 1–UVRAG interaction: FLAG-UVRAG pulled down significantly more endogenous Beclin 1 when Tat-SP4 was added to the cell lysate, but no such effect was observed for Tat-SC4 (Fig. 5*I*).

In summary, using the structures of the Beclin 1–UVRAG coiled-coil complex and the Beclin 1 coiled-coil homodimer as guidance, we designed a series of stapled peptides that bind to the Beclin 1 coiled-coil domain with high affinity in vitro. One such designed peptide, Tat-SP4, effectively reduces Beclin 1 self-association and promotes the Beclin 1–Atg14L/UVRAG interaction in vivo.

The Designed Beclin 1-Specific Stapled Peptide Induces Autophagy and Significantly Enhances Endolysosomal Degradation of EGFR. The efficacy of the designed peptide Tat-SP4 in modulating autophagy and endolysosomal degradation of EGFR was characterized using

cell-based assays. We added Tat-SP4 to HeLa cells stably expressing GFP-LC3 and did confocal imaging studies. Treatment with Tat-SP4, but not Tat-SC4, increased the GFP-LC3 dot numbers (autophagosomes) by approximately twofold, in both the presence and absence of CQ (Fig. 6 *A* and *B*). We also used Rhodamine-labeled SP4 (Rho-SP4) to track the cell membrane penetration and cytoplasmic distribution of the stapled peptide. Our imaging results show that Rho-SP4 readily penetrated the cell membrane of HeLa GFP-LC3 cells and was distributed almost exclusively in the cytosol after 30 min of treatment (Fig. 6*C*). Rho-SP4 formed puncta that partially overlapped endogenous LC3, GFP-LC3 puncta, and LysoTracker dots (Fig. 6 *C* and *D* and *SI Appendix*, Fig. S7*A*). Additionally, we also tested the colocalization of Beclin 1 and Rho-SP4 by transfecting Beclin 1-GFP into A549 cells. Our data reveal that upon Rho-SP4 treatment, transiently expressed Beclin 1 formed puncta that partially overlapped Rho-SP4 puncta. In contrast, under Rho-SC4 treatment, Beclin 1 failed to form puncta and instead was distributed in a diffuse manner in the cytosol (*SI Appendix*, Fig. S7 *B* and *C*). These observations suggest that SP4 is intimately involved with autophagy machineries and enhances autophagic activity.

The impact of Tat-SP4 on cellular autophagic activity was characterized further by Western blots of LC3 and p62. We first used a 3-[4,5-dimethylthiazol-2-yl]-2,5-diphenyltetrazolium bromide (MTT) assay to confirm that Tat-SP4, together with the control peptide Tat-SC4, showed negligible cytotoxicity for HEK293T and A549 cells at 12.5- and 25-μM concentrations after 5 h of treatment (*SI Appendix*, Fig. S8). In HEK293T cells, the addition of Tat-SP4 to cell medium at a 10-μM concentration led to an approximately twofold increase in the LC3-II level, and this increase reached approximately threefold when the higher concentration of 20 μM was used (Fig. 6 *E* and *G*). The p62 level was also reduced by ∼50% under Tat-SP4 treatment (Fig. 6 *E* and *I*). The addition of CQ intensified the effect on LC3-II levels, with an approximately threefold increase when Tat-SP4 was added at 10 μM and an approximately fivefold increase when Tat-SP4 was added at 20 μM (Fig. 6 *F* and *H*). These findings suggest that Tat-SP4 can effectively induce autophagy and increase autophagic flux. On the other hand, CQ treatment elevated the p62 level, even with Tat-SP4 treatment (Fig. 6 *F* and *J*). This is in agreement with CQ's role as a lysosomal inhibitor that stalls the autophagy process at the final stage of lysosomal degradation. Thus, the promoting effect of Tat-SP4 appears to target the early stage of Vps34-dependent autophagy and endocytic trafficking but not the late stage of lysosomal degradation.

We also tested the efficacy of Tat-SP4 in promoting endolysosomal trafficking by measuring the EGFR degradation rate after Tat-SP4 treatment in multiple cell lines. In HEK293T cells, treatment by Tat-SP4 at a 20-μM concentration led to a significant enhancement in EGFR degradation, with only ∼30% remaining at 60 min post EGF stimulation in contrast to ∼75% detected under saline (control) or Tat-SC4 treatment at 20 μM (Fig. 7 *A* and *D*). In A549 NSCLC cells the EGFR level is highly stable, and no degradation was detected 5 h after EGF stimulation with saline (control) or Tat-SC4 treatment (Fig. 7 *B* and *E*). This baseline profile is steadier than that observed under vector-expressing conditions (Fig. 4 *D* and *F*). Similar variation has been observed in previous studies with vector-expressing treatment leading to more EGFR degradation (25–28). Nonetheless, the addition of Tat-SP4 to A549 cell medium at 20 μM led to a significant enhancement in EGFR degradation, with ∼75% remaining at 2 h and ∼25% at 5 h (Fig. 7 *B* and *E*). We further tested the effect of Tat-SP4 on the TKI-insensitive NSCLS cell line H1975. As in A549 cells, EGFR is overexpressed and highly stable in H1975 cells over the prolonged period of 20 h (Fig. 7 *C* and *F*). Treatment by Tat-SP4 induced robust enhancement of EGFR degradation, with ∼50% degradation at 15 h after EGF stimulation, while Tat-SC4 showed no effect (Fig. 7 *C* and *F*).

Collectively, our data confirm that the rationally designed Beclin 1-targeting stapled peptide Tat-SP4 can induce autophagy and significantly enhances the endolysosomal degradation of EGFR in multiple cell lines. The enhancement of EGFR degradation is particularly prominent in cell lines that have robust overexpression of EGFR.

Discussion

Potent interaction between Beclin 1 and its binding partners Atg14L or UVRAG is essential for the dynamic transition of Beclin 1 from its functionally inactive self-associated form to Atg14L- or UVRAG-containing Beclin 1–Vps34 subcomplexes to promote Vps34-dependent autophagy and endolysosomal trafficking (4–7, 18).

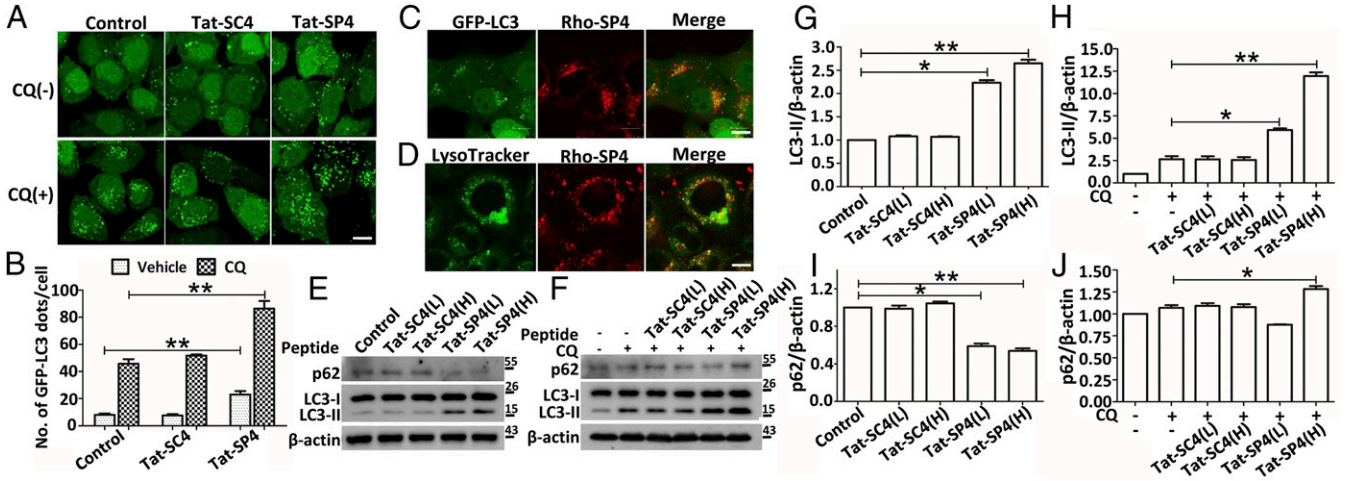

Fig. 6. Beclin 1-specific stapled peptide promotes autophagy. (*A*) Representative confocal fluorescence images of HeLa cells stably expressing GFP-LC3 after treatment with vesicle water (control), Tat-SC4, or Tat-SP4 for 3 h. Experiments were done both in the absence (–) and presence (+) of 25 μM CQ. (Scale bar: 10 μm.) (*B*) Histogram showing the quantification of the results from *A* performed by counting the number of GFP-LC3 puncta per cell. Bars represent mean ± SEM ($n = 3$). *$P < 0.05$, **$P < 0.01$; *t* test. (*C*) Representative confocal fluorescence images of HeLa cells stably expressing GFP-LC3 after treatment with Rho-SP4 for 3 h. LC3 puncta overlap with Rho-SP4 dots. (Scale bar: 10 μm.) (*D*) Representative confocal fluorescence images of HeLa cells after treatment with Rho-SP4 and LysoTracker dye. Rho-SP4 dots overlap well with lysosomes marked by LysoTracker. (Scale bar: 10 μm.) (*E* and *F*) Western blots to assess the LC3 lipidation profile and p62 level in HEK293T cells after treatment with low (10 μM, L) and high (20 μM, H) concentrations of Tat-SC4 or Tat-SP4) without (*E*) or with (*F*) CQ for 3 h. (*G–J*) Quantification of LC3 lipidation profiles (*G* and *H*) and p62 levels (*I* and *J*) from data in *E* and *F*. The levels of LC3-II or p62 were normalized to the β-actin level. Data are presented as mean ± SEM ($n = 3$). *$P < 0.05$, **$P < 0.01$; *t* test.

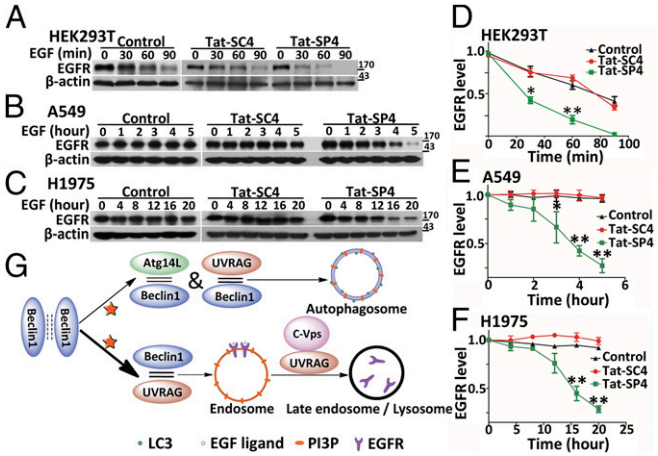

Fig. 7. The Beclin 1-specific stapled peptide Tat-SP4 significantly enhances EGFR degradation. (*A–C*) The impact of Tat-SP4 on EGFR degradation was assessed using three different cell lines: HEK293T (*A*) and two NSCLC cell lines, A549 (*B*) and H1975 (*C*). Cells were starved overnight and were treated with 200 ng/mL EGF together with 20 μM of peptide (Tat-SC4 or Tat-SP4) for the indicated times. The EGFR level in cell lysates was analyzed by Western blots at specific time points. (*D–F*) Time-dependent plots to quantify the EGFR degradation profiles in HEK293T (*D*), A549 (*E*), and H1975 (*F*) cells after three independent experiments for each cell line. The level of EGFR was normalized to the β-actin level at different time points and was further normalized to time 0, when ligand EGF was added. Values represent the mean ± SEM ($n = 3$). $^{*}P < 0.05$, $^{**}P < 0.01$; *t* test. (*G*) Diagram showing the design of our scheme of targeting the Beclin 1 coiled-coil domain with a designed peptide. The dashed lines represent the imperfect interface for the Beclin 1 coiled-coil homodimer. The solids lines represent the Beclin 1–Atg14L or –UVRAG coiled-coil interface, with thicker lines indicating stronger binding affinity. Star shapes represent the designed peptide. It binds to the Beclin 1 coiled-coil domain, reduces its self-association, and promotes the Beclin 1–Atg14L or –UVRAG interaction, resulting in an increase in both autophagy and endolysosomal trafficking.

To facilitate such transition, it is imperative that the Beclin 1–Atg14L or –UVRAG interaction, as mediated by their respective coiled-coil domains, be more potent than the Beclin 1 self-association. Here our crystal structure of the Beclin 1–UVRAG coiled-coil complex reveals a heterodimeric interface significantly strengthened by both canonical hydrophobic pairings and non-canonical electrostatically complementary interactions. The Beclin 1–UVRAG interface contains almost the same set of leucine zipper pairs as the imperfect and metastable Beclin 1 coiled-coil homodimer reported previously (18). Additionally, the Beclin 1–UVRAG coiled-coil complex is strengthened by one extra leucine zipper pair (L210*d*–L264*d*′) and one electrostatically complementary ion pair (R203*d*–E260*a*′) that replace the corresponding imperfect pairings seen at the Beclin 1 homodimer interface. Thus, the imperfect residues of Beclin 1 and UVRAG coiled-coil domains, through sequence complementarity, become the defining features rendering the Beclin 1–UVRAG interaction more potent than the Beclin 1 homodimer. We speculate that a similar mechanism may also apply to the Beclin 1–Atg14L interaction; i.e., complementarity between imperfect Beclin 1 and Atg14L residues would favor their heterodimeric coiled-coil assembly over the functionally inactive Beclin 1 homodimer. Additionally, Beclin 2, a recently identified homolog of Beclin 1 with a distinct functional profile, contains a coiled-coil domain that is highly similar to that of Beclin 1, with an imperfect and metastable interface (29, 30). We propose the Beclin 2–Atg14L/UVRAG coiled-coil interface may be strengthened by both hydrophobic and electrostatically complementary pairings as well.

Our structure-guided functional studies demonstrate that the potency of the Beclin 1–UVRAG coiled-coil interaction is critical for promoting Vps34-dependent endosomal trafficking. Only UVRAG constructs that have strong binding affinity for Beclin 1 and can outcompete Atg14L in recruiting endogenous Beclin 1, i.e., the wild type and the 1E and 2E mutants, can effectively promote lysosomal degradation of EGFR under overexpressed conditions. The UVRAG mutants 5E and 6E fail to do so even though they retain association with Beclin 1 in vivo. Our previous study has proposed that excessive amounts of Beclin 1 may exist as a reserve pool in a functionally inactive homodimeric form (18, 19). Overexpressed UVRAG with stronger binding affinity may outcompete Atg14L in recruiting endogenous Beclin 1 to promote Vps34-dependent processes such as endocytic trafficking. By the same argument, overexpression of UVRAG offers limited benefit to the autophagy process because the higher abundance of the UVRAG-containing Beclin 1–Vps34 complex would come at the expense of the competitive Atg14L-containing complex.

UVRAG is a multivalent effector of the endocytic trafficking process and can exert a regulatory effect through at least two distinct routes. On one hand, the UVRAG-containing Beclin 1–Vps34 complex can lead to increased PI3P production and assist in the maturation of EGFR-containing endosomes (3, 7, 28). On the other hand, UVRAG also interacts with the class C Vps complex to promote fusion of autophagosomes or early endosomes with late endosomes/lysosomes to enhance lysosomal degradation of EGFR (8, 31). These two interactions are genetically separable, because UVRAG binds to Beclin 1 via its coiled-coil domain but uses its N-terminal C2 domain to interact with the class C Vps complex (8). However, the relationship between these two routes is not clear. In our study, all UVRAG Leu-to-Glu mutants are expected to retain their interaction with the class C Vps complex, as the mutations are exclusively in the coiled-coil region and would leave the C2 domain intact. Hence their distinct phenotypes in regulating endolysosomal degradation of EGFR should arise solely from their different binding affinities to Beclin 1. The enhancement effect observed in the 1E and 2E mutants suggests that the potent Beclin 1–UVRAG interaction exerts a dominant role in promoting endocytic trafficking function while the class C Vps-UVRAG interaction does not.

Finally, there has been growing interest in targeting the autophagy process for disease-modifying therapies. Multiple clinical trials were initiated using the autophagy inhibitor CQ in combination with existing cancer drugs to enhance therapeutic efficacy for late-stage refractory cancer types (32). However, potent and specific modulators of autophagy are lacking because compounds such as CQ and inhibitors for mTOR or Vps34 may affect many processes in addition to autophagy. A previous study reported that a Beclin 1 peptide derived from its membrane-binding region could serve as a potent inducer of autophagy and reduce the replication of pathogens in cell- and animal-based models (33). Here we present a strategy of autophagy modulation that influences the dynamic redistribution of Beclin 1 into its biochemically and functionally distinct subcomplexes. By specifically binding to the C-terminal region of the Beclin 1 coiled-coil domain, a rationally designed peptide with hydrocarbon stapling to stabilize its α-helical structure can bind to the Beclin 1 coiled-coil domain, reduce its self-association, and promote the formation of Atg14L/UVRAG-containing Beclin 1–Vps34 complexes (Fig. 7*G*). As a result, both Vps34-dependent autophagy and endocytic trafficking can be enhanced. Notably, our designed peptide induces a significant enhancement of EGFR degradation in NSCLC cell lines that have robust EGFR overexpression, a result not reported for the Beclin 1-derived peptide from the previous study. Given that Beclin 1 shows frequent monoallelic deletion in various cancer types, our designed peptides may provide a plausible approach to increase Beclin 1 function, attenuate EGFR signaling, and suppress cancer cell proliferation by enhancing the Beclin 1–UVRAG interaction. Furthermore, because recent studies have implicated the UVRAG-containing Beclin 1–Vps34 complex in the endocytic degradation of multiple membrane receptors such as insulin receptor and the TGF-β receptor ALK5 (34, 35), our design strategy of targeting Beclin 1 for regulation may be applicable to these processes as well. Therefore, our stapled peptides not only can be used as a tool to probe Beclin

1–Vps34–dependent autophagy and lysosome degradation in various cellular processes but also should be explored for therapeutic potential in targeting the diseases associated with impairment of autophagy or endolysosomal trafficking.

Materials and Methods

Crystallization and Structure Determination. Crystals of the Beclin 1–UVRAG–linked construct were grown at 16 °C by the hanging-drop vapor-diffusion method mixing 1 μL of Beclin 1–UVRAG protein at 20 mg/mL with 1 μL of reservoir solution containing 3.0 M NaCl and 100 mM citric acid buffer (pH 3.5). The Au derivative was obtained by soaking crystals in reservoir solution containing 5 mM $KAu(CN)_2$ for about 10 s. The crystals were cryoprotected with 20% ethylene glycol before being mounted onto the X-ray source. Initial crystals were screened in-house using a Rigaku X-ray diffraction system with an R-axis image plate and a PILATUS 200K hybrid pixel-array detector. Crystals with good diffraction quality were then taken to beamline BL17U1 at the Shanghai Synchrotron Radiation Facility in Shanghai, People's Republic of China. Statistics are summarized in *SI Appendix*, Table S1. The coordinates of the Beclin 1–UVRAG complex have been deposited to Protein Data Bank (PDB ID code 5YR0).

In Vitro Competition Assay. Purified coiled-coil fragments of His-tagged Beclin 1 and Atg14L were mixed at a 1:1 molar ratio in binding buffer (20 mM NaP, 500 mM NaCl, pH 7.4). Purified UVRAG coiled-coil fragments were individually added to the His-tagged Beclin 1–Atg14L mixture at increasing molar ratios of 0.5:1:1, 1:1:1, and 2:1:1 and were incubated at 4 °C for 30 min. The Beclin 1–Atg14L–UVRAG mixture was then subjected to standard procedures of the pull-down experiment using Ni^{2+}-nitrilotriacetic acid (NTA) agarose beads. After thorough washing, the bound protein was eluted by SDS sample buffer and analyzed by SDS/PAGE.

EGFR Degradation Assay. HEK293T, A549, or H1975 cells in six-well plates were washed twice with PBS and were serum-starved overnight in DMEM. EGFR endocytosis was induced by incubation with DMEM (with 20 mM Hepes and 0.2% BSA) containing 200 ng/mL EGF (Invitrogen). Cells were collected at each time point after EGF stimulation and were lysed. Twenty micrograms of protein lysate were resolved by SDS/PAGE and immunoblotted with anti-EGFR antibody (1:2,000; Santa Cruz Biotechnology).

Computational Design of Stapled Peptides. The 3D structure of the α-helical segment corresponding to residues 191–205 within the Beclin 1 coiled-coil domain (PDB ID code 3Q8T) was used as the initial model for SP1. Eleven other SPs (i.e., SP2–SP12) were designed by substituting the residues at positions 191, 194, 195, 201, and 205. A hydrocarbon staple of 11-carbon length was added to link residues 197 and 204. The N terminus of each stapled peptide was capped with an acetyl group, and the C terminus was capped with a methylamide group. All the above molecular modeling tasks were conducted using Sybyl software version 8.0 (Certara). Molecular dynamics simulations were conducted using the AMBER software version 14 (University of California, San Francisco) to compute the binding energies of all designed SPs to Beclin-1.

Synthesis of Regular and Stapled Peptide SP4. The scrambled peptides and stapled peptide candidates deemed promising by computational design were acquired commercially from Shanghai Abbiochem Co., Ltd. The chemical structure and purity of the final synthesized product were characterized by high-resolution MS and HPLC. All samples are readily water-soluble. Peptide stock (20 mM) was made by dissolving samples in H_2O.

Details regarding reagents, plasmids, mammalian cell culture, immunoblotting, fluorescent microscopy, ITC, and software used for X-ray crystallography or molecular dynamics simulations can be found in *SI Appendix*, *Supplementary Methods and Materials*.

ACKNOWLEDGMENTS. We thank the Shanghai Synchrotron Radiation Facility beam line BL17U for help with data collection and the University Research Facility in Life Sciences, Hong Kong Polytechnic University, for providing technical support and access to the confocal microscope. The work was supported by Research Grants Council of Hong Kong Grants PolyU 151043/14M, PolyU 151052/16M, PolyU 151015/17M, N-PolyU503/16, C5030-14E, and AoE/M-09/12, Hong Kong Innovation and Technology Support Program Grant ITS/177/14, and Shenzhen Basic Research Program of China Grant JCYJ20160531184305919 (to Y.Z.); Science and Technology Planning Project of Guangdong Province of China Grant 2015A010107002 (to W.Y.); National Natural Science Foundation of China Grant 31200563 and Shenzhen Basic Research Program of China Grant JCYJ20140819153305695 (to X.L.); National Medical Research Council Singapore Clinician Scientist-Individual Research (NMRC-CIRG) Grants1346/2012 and 1373/2013 (to H.-M.S.); and NIH/National Institute of Neurological Disorders and Stroke Grant R01NS060123 (to Z.Y.).

1. Funderburk SF, Wang QJ, Yue Z (2010) The Beclin 1-VPS34 complex–At the crossroads of autophagy and beyond. *Trends Cell Biol* 20:355–362.
2. Itakura E, Mizushima N (2009) Atg14 and UVRAG: Mutually exclusive subunits of mammalian Beclin 1-PI3K complexes. *Autophagy* 5:534–536.
3. Itakura E, Kishi C, Inoue K, Mizushima N (2008) Beclin 1 forms two distinct phosphatidylinositol 3-kinase complexes with mammalian Atg14 and UVRAG. *Mol Biol Cell* 19:5360–5372.
4. Zhong Y, et al. (2009) Distinct regulation of autophagic activity by Atg14L and Rubicon associated with Beclin 1-phosphatidylinositol-3-kinase complex. *Nat Cell Biol* 11: 468–476.
5. Matsunaga K, et al. (2009) Two Beclin 1-binding proteins, Atg14L and Rubicon, reciprocally regulate autophagy at different stages. *Nat Cell Biol* 11:385–396.
6. Sun Q, et al. (2008) Identification of Barkor as a mammalian autophagy-specific factor for Beclin 1 and class III phosphatidylinositol 3-kinase. *Proc Natl Acad Sci USA* 105: 19211–19216.
7. Liang C, et al. (2006) Autophagic and tumour suppressor activity of a novel Beclin1-binding protein UVRAG. *Nat Cell Biol* 8:688–699.
8. Liang C, et al. (2008) Beclin1-binding UVRAG targets the class C Vps complex to coordinate autophagosome maturation and endocytic trafficking. *Nat Cell Biol* 10: 776–787.
9. Fimia GM, et al. (2007) Ambra1 regulates autophagy and development of the nervous system. *Nature* 447:1121–1125.
10. Pattingre S, et al. (2005) Bcl-2 antiapoptotic proteins inhibit Beclin 1-dependent autophagy. *Cell* 122:927–939.
11. Lu J, et al. (2014) NRBF2 regulates autophagy and prevents liver injury by modulating Atg14L-linked phosphatidylinositol-3 kinase III activity. *Nat Commun* 5:3920.
12. He C, Levine B (2010) The Beclin 1 interactome. *Curr Opin Cell Biol* 22:140–149.
13. Baskaran S, et al. (2014) Architecture and dynamics of the autophagic phosphatidylinositol 3-kinase complex. *eLife* 3:e05115.
14. Stjepanovic G, Baskaran S, Lin MG, Hurley JH (2017) Vps34 kinase domain dynamics regulate the autophagic PI 3-kinase complex. *Mol Cell* 67:528–534.e3.
15. Rostislavleva K, et al. (2015) Structure and flexibility of the endosomal Vps34 complex reveals the basis of its function on membranes. *Science* 350:aac7365.
16. Young LN, Cho K, Lawrence R, Zoncu R, Hurley JH (2016) Dynamics and architecture of the NRBF2-containing phosphatidylinositol 3-kinase complex I of autophagy. *Proc Natl Acad Sci USA* 113:8224–8229.
17. Ohashi Y, et al. (2016) Characterization of Atg38 and NRBF2, a fifth subunit of the autophagic Vps34/PIK3C3 complex. *Autophagy* 12:2129–2144.
18. Li X, et al. (2012) Imperfect interface of Beclin1 coiled-coil domain regulates homodimer and heterodimer formation with Atg14L and UVRAG. *Nat Commun* 3:662.
19. Li X, He L, Zhang M, Yue Z, Zhao Y (2012) The BECN1 coiled coil domain: An "imperfect" homodimer interface that facilitates ATG14 and UVRAG binding. *Autophagy* 8:1258–1260.
20. Kim J, et al. (2013) Differential regulation of distinct Vps34 complexes by AMPK in nutrient stress and autophagy. *Cell* 152:290–303.
21. Cromm PM, Spiegel J, Grossmann TN (2015) Hydrocarbon stapled peptides as modulators of biological function. *ACS Chem Biol* 10:1362–1375.
22. Walensky LD, Bird GH (2014) Hydrocarbon-stapled peptides: Principles, practice, and progress. *J Med Chem* 57:6275–6288.
23. Verdine GL, Hilinski GJ (2012) Stapled peptides for intracellular drug targets. *Methods Enzymol* 503:3–33.
24. Kim YW, Grossmann TN, Verdine GL (2011) Synthesis of all-hydrocarbon stapled α-helical peptides by ring-closing olefin metathesis. *Nat Protoc* 6:761–771.
25. Kim YM, et al. (2015) mTORC1 phosphorylates UVRAG to negatively regulate autophagosome and endosome maturation. *Mol Cell* 57:207–218.
26. Xu D, et al. (2015) Modification of BECN1 by ISG15 plays a crucial role in autophagy regulation by type I IFN/interferon. *Autophagy* 11:617–628.
27. Zeng X, Overmeyer JH, Maltese WA (2006) Functional specificity of the mammalian Beclin-Vps34 PI 3-kinase complex in macroautophagy versus endocytosis and lysosomal enzyme trafficking. *J Cell Sci* 119:259–270.
28. McKnight NC, et al. (2014) Beclin 1 is required for neuron viability and regulates endosome pathways via the UVRAG-VPS34 complex. *PLoS Genet* 10:e1004626.
29. He C, et al. (2013) Beclin 2 functions in autophagy, degradation of G protein-coupled receptors, and metabolism. *Cell* 154:1085–1099.
30. Su M, et al. (2017) BECN2 interacts with ATG14 through a metastable coiled-coil to mediate autophagy. *Protein Sci* 26:972–984.
31. Pirooz SD, et al. (2014) UVRAG is required for virus entry through combinatorial interaction with the class C-Vps complex and SNAREs. *Proc Natl Acad Sci USA* 111: 2716–2721.
32. Barnard RA, et al. (2014) Phase I clinical trial and pharmacodynamic evaluation of combination hydroxychloroquine and doxorubicin treatment in pet dogs treated for spontaneously occurring lymphoma. *Autophagy* 10:1415–1425.
33. Shoji-Kawata S, et al. (2013) Identification of a candidate therapeutic autophagy-inducing peptide. *Nature* 494:201–206.
34. Nemazanyy I, et al. (2015) Class III PI3K regulates organismal glucose homeostasis by providing negative feedback on hepatic insulin signalling. *Nat Commun* 6:8283.
35. O'Brien CE, Bonanno L, Zhang H, Wyss-Coray T (2015) Beclin 1 regulates neuronal transforming growth factor-β signaling by mediating recycling of the type I receptor ALK5. *Mol Neurodegener* 10:69.